

Plasma Source Development for Plasma Wakefield Acceleration

by

Ruaa Al-Harthy

Advisor:

Professor Micheal Litos, Department of Physics

Committee Members:

Professor John Cumalat, Department of Physics

Professor James Meiss, Department of Applied Mathematics

Professor Adam Norris, Department of Applied Mathematics

UNIVERSITY OF COLORADO BOULDER

DEPARTMENT OF PHYSICS PHYSICS

DEFENDED APRIL 11, 2023

Abstract

Conventional high energy particle accelerators tend to be extremely large, making them expensive and challenging to build. Electron beam driven Plasma Wakefield Accelerators (PWFA), on the contrary, provide “high gradient acceleration” which means particles can attain high energy in a short distance, allowing the accelerator to be much more compact. In a PWFA, an electron bunch travels through a plasma, driving a wake behind it. A second electron bunch travels shortly behind the first, being accelerated by the strong electric fields in the plasma wake. Research at facilities such as FACET at SLAC National Accelerator Laboratory have demonstrated the efficacy of the PWFA for acceleration. The next step is to simultaneously maintain the quality of the electron bunch during the acceleration process. This requires a specific plasma density profile, which is best produced by laser ionization of gas. The research presented here is a study of a novel optical configuration that may provide a simple, inexpensive, and robust means of focusing a laser pulse to produce the ideal PWFA plasma source.

Acknowledgements

I would like to express my special thanks of gratitude to my advisor Prof. Michael Litos who gave me this golden opportunity to work in research with his amazing team of students whom I would also like to direct my thankfulness to for providing the best learning environment I've ever experienced. I would like to thank my family, especially my parents for supporting me throughout this journey.

Contents

1	Introduction	1
1.1	Background	1
1.2	Plasma Wakefield Acceleration (PWFA)	3
1.3	Plasma Source	4
2	Plasma Formation	8
2.1	Types of Ionization	8
2.2	Laser Ionization	11
3	Motivation	13
3.1	FACET II	13

3.2	Tandem Lens Scheme	15
3.3	Axicons Lens Scheme	16
4	Optics Of Axicons	18
4.1	Axicon Focusing	18
4.2	Optical Kerr Effect	22
5	Experimental Setup and Methods	24
5.1	Triple Axicon Design	24
5.2	Experimental Setup	27
5.3	Method of Studying Alignment Tolerance	29
6	Data and Results	32
6.1	Best Alignment Laser Profile	32
6.2	Tolerance Studies Results	38
7	Conclusions and Future Work	40
7.1	Conclusions	40

7.2	Potential Issues	40
7.3	Future Work	42
	Bibliography	42

Figures

1.1	Schematic of a wakefield driven by an electron drive bunch. The drive bunch (right) drives the wake in the plasma (purple), accelerating the witness bunch (left). Both bunches travel to the right at relativistic speed.	3
1.2	Capacitor model of oscillating electron layer in a perturbed plasma. . .	5
2.1	Different types of ionization [6]. Left: photo-ionization. Middle: tunnel ionization. Right: barrier suppression ionization.	11
3.1	Overhead photo of the FACET-II facility at SLAC National Accelerator Laboratory. Image taken from https://facet-ii.slac.stanford.edu/	14
3.2	CAD drawing of the FACET-II accelerator tunnel. Image taken from https://facet-ii.slac.stanford.edu/	14

3.3	Schematic of the tandem lens focusing technique. The first lens (ρ) shapes the transverse donut intensity profile and the second lens (r) removes the residual phase from the first lens. The plasma forms at the shaded grey region downstream of the second lens where the Bessel beam is formed [11].	16
4.1	Ray tracing schematic of the focusing pattern of an axicon lens.	18
4.2	Axial intensity profile of a Bessel beam formed by a flat-top laser beam when focused by an axicon lens.	20
4.3	Axial intensity profile (a), transverse intensity profile (b), and transverse intensity lineout (c) produced by a super-Gaussian laser beam focused by an axicon lens.	22
5.1	Schematic of the triple axicon design. The first two axicons form a telescope that creates a donut-shaped beam which is focused a distance d_2 downstream from the third axicon. The telescope axicons are characterized by the same angle α_1 and the third axicon is characterized by angle α_2	25

5.2	Experimental setup schematic. The HeNe laser has the expander attached to it (small square from which the laser beam is emitted). L_1 and L_2 are convex lenses. A_1 , A_2 and A_3 are axicons. The camera sits atop a rail on which it can move along the laser propagation axis.	28
5.3	Photograph of the experimental setup in the CU Boulder laser lab. . .	29
5.4	Testing for vertical displacement of the optics. The orange line in each image represents the height measurement of the optic. The first image shows that the original height of the axicon is ~ 10 cm. The second image shows the height of the axicon to be ~ 10.2 cm (2mm displacement). The third image shows the height of the axicon to be ~ 10.4 cm (4mm displacement).	30
5.5	Testing for angular displacement of the optics. A stick was taped to the axicon to tell which direction it faced in optimal alignment. Protractor software was used to measure the angle in the images. The directions of the two axicons are highlighted with dashed orange lines.	31
6.1	Transverse intensity profile for the Bessel beam under optimal alignment conditions measured at $z=35$ cm (35cm downstream from the third axicon). This corresponds to the position of the peak intensity.	32

6.2	Transverse intensity profile for the Bessel beam (top left). Plots generated by taking the lineout across the (a) row and (b) column that have the highest intensity (pixel count).	33
6.3	Horizontal (a) and vertical(b) intensity lineouts (solid lines) of the optimized Bessel beam profile taken from 6.1. A fit to the Bessel profile is shown (orange dashed lines) in each, with a result of $\alpha = 1.3^\circ$ in both plots.	34
6.4	Measured longitudinal intensity profile of the Bessel as measured along the length of the camera rail. The vertical dashed lines indicate the start and end of the expected Bessel beam (orange vertical lines) and the actual resultant Bessel beam (green vertical lines).	36
6.5	FWHM of the central Bessel lobe as measured along the z-axis using horizontal (a) and vertical (b) lineouts.	37
6.6	Laser intensity profile measurements for various vertical displacements of the third axicon.	38
6.7	Summary of the major findings of the experiment.	39

7.1 Schematic of the new double axicon design. The first axicon defocuses the light into a donut-shaped beam which is then focused a distance d_2 downstream from the second axicon. Axicon $A1$ is characterized by angle α_1 and axicon $A2$ is characterized by angle α_2 42

Chapter 1

Introduction

1.1 Background

Particle accelerators have been used for decades to explore the answers for profound physics questions about our existence. These accelerators are huge metallic structures that provide the necessary electric fields to accelerate particles to speeds close to the speed of light and then collide them in the center of a sophisticated particle detector. The products of such energetic collisions are then studied and analyzed by high energy physicists in a quest to learn more about fundamental particles and fields that may tell us something about the early universe. As they get closer to solving those mysteries, they require even more powerful accelerators [1]. As of now, the largest conventional particle accelerator is the Large Hadron Collider (LHC) operated by CERN which is

located near the French-Swiss border in Geneva, Switzerland. The LHC has successfully accelerated particles to energies up to 6.5 TeV, creating collisions with center-of-mass energies of 13 TeV.

Unfortunately, there are limitations that exist with the technologies that we have today [1]. One being funding and land space, since building gigantic accelerators can cost billions of dollars and tens of square kilometers of land. The second is the fact that there is a threshold to the maximum electric field that can be created without causing any damage to a conventional metallic accelerating structure of around 100 MV/m, corresponding to an accelerating gradient of 100 MeV/m. This was the motivation behind the idea of accelerating particles in a plasma medium instead, because plasmas are the most broken down form matter.

The concept of plasma based accelerators was first proposed by Toshiki Tajima and John Dawson in 1979 [1]. The underlying idea is to accelerate charged particles using the strong fields that can occur in plasma waves. Plasma-based accelerators are generated either by a laser pulse, hence the name “Laser Wakefield Accelerator (LWFA)” or a relativistic particle beam, referred to as “Plasma Wakefield Accelerator (PWFA)”.

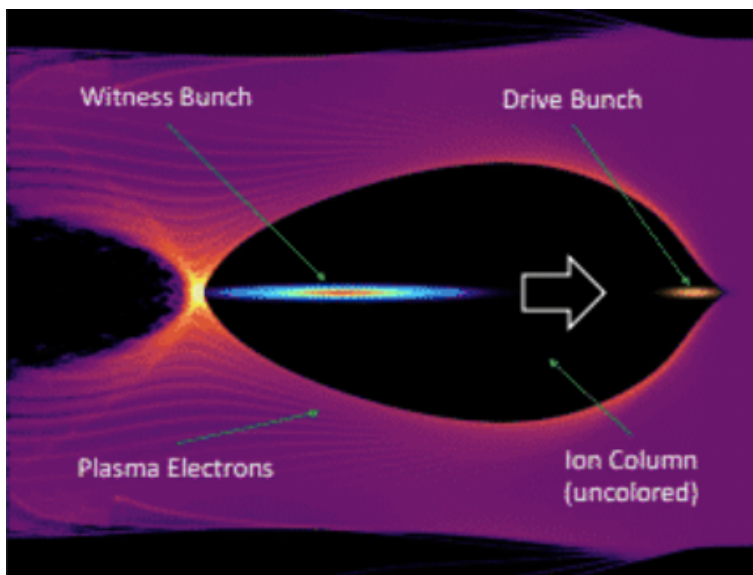


Figure 1.1: Schematic of a wakefield driven by an electron drive bunch. The drive bunch (right) drives the wake in the plasma (purple), accelerating the witness bunch (left). Both bunches travel to the right at relativistic speed.

1.2 Plasma Wakefield Acceleration (PWFA)

The idea of accelerating charged particles in wakefields driven by a bunch of relativistic particles (as opposed to an intense laser pulse) was first theoretically proposed in 1985 and experimentally demonstrated in 1988 [2].

The electron bunch that is used to induce the wakefield is usually referred to as the drive beam or drive bunch and the electron bunch that is accelerated by the wakefield is called the witness beam or the witness bunch. Both bunches must be relativistic, but do not have to have the same energy. The drive bunch is first sent into the plasma to create the wakefield by repelling the electrons outwards leaving ions behind. The ions, in turn, pull the plasma electrons behind the beam back in, thus forming an electron

bubble around the positive region of nearly stationary ions. The electric field inside the wake points radially outwards from the center. As the drive beam moves forward, the wake structure follows it at nearly the speed of light. The witness bunch follows immediately after the drive bunch in the rear of the wake, gaining energy from the electric field [2].

In 2007, experiments at SLAC National Accelerator Laboratory successfully accelerated electrons in the tail of a single long bunch from 42 GeV to 85 GeV in an 85 cm long plasma filament, which corresponds to an accelerating gradient of around 50 GeV/m [2], over two orders of magnitude larger than the metallic accelerator breakdown limit.

The high accelerating gradients of PWFA devices imply that high-energy accelerators may be able to be built more compact and thus less expensive in the future, making it more feasible to continue to study particle physics at the energy frontier for decades more to come.

1.3 Plasma Source

There are characteristics that we would like the plasma to have, and in order to understand how to achieve them, we have to understand how plasma responds to external disturbance, which in our case is a laser pulse. Plasmas are generally assumed

to be quasi-neutral, which means that they have equal numbers of positively charged and negatively charged particles. When a quasi-neutral plasma gets disturbed by a laser pulse, a layer of electrons gets displaced by some distance x . Since the positively charged ions are much more massive than electrons, we can assume that they don't move when the plasma is disturbed. When the electrons get displaced, they exhibit an oscillatory behavior around the slightly more positive region. We can find the frequency of the electrons by imagining that the electron layer creates a capacitor whose plates are distance x apart as shown in Figure 1.2 [3].

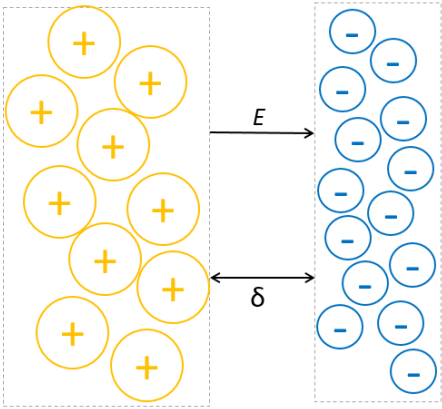


Figure 1.2: Capacitor model of oscillating electron layer in a perturbed plasma.

The surface charge of the two imaginary plates are $\sigma = \pm en_e x$, where n_e is the charge density. Hence, the resulting electric field is:

$$\mathbf{E} = \frac{\sigma}{\epsilon_0} = \frac{en_e x}{\epsilon_0}$$

By Newton's second law, we get:

$$\mathbf{F}_{net} = \mathbf{E}$$

$$m_e \frac{dv}{dt} = -m_e \frac{d^2x}{dt^2} = -eE = \frac{e^2 n_e x}{\epsilon_0}$$

Where m_e is the mass of the electron. By rearranging the equation we get:

$$\begin{aligned} m_e \frac{d^2x}{dt^2} + \frac{e^2 n_e}{\epsilon_0} x &= 0 \\ \frac{d^2x}{dt^2} + w_p^2 x &= 0 \\ w_p &= \left(\frac{e^2 n_e}{m_e \epsilon_0} \right)^{1/2} \end{aligned} \tag{1.1}$$

w_p is called *electron plasma frequency*.

Now, we can use the dispersion relation to find the refractive index to understand how laser pulses interact with plasma. The dispersion relation in plasma is:

$$w^2 = w_p^2 + c^2 k^2 \tag{1.2}$$

The refractive index is:

$$\eta = \frac{ck}{w} = \left(1 - \frac{w_p^2}{w^2} \right)^{1/2} \tag{1.3}$$

As we can see from Equation 1.3 when $w_p < w$, the value of the refractive index is positive and less than 1. Such plasmas are called *underdense plasmas* and we can deduce some important features of electromagnetic waves propagation using the following equations for phase velocity and group velocity:

$$v_p = \frac{w}{k} \approx c \left(1 + \frac{w_p^2}{2w^2} \right) > c \tag{1.4}$$

$$v_g = \frac{\partial w}{\partial k} \approx c \left(1 - \frac{w_p^2}{2w^2} \right) < c \tag{1.5}$$

Hence, the speed of the laser pulse tends to decrease. However, when $w_p > w$ the refractive index becomes imaginary and the electromagnetic waves become evanescent. Such *overdense plasmas* will reflect the laser pulse [3].

Chapter 2

Plasma Formation

2.1 Types of Ionization

We create our lab plasma from ionized gas. The typical pressures of a gas are around $10^{-3} - 1$ atm. Since the plasma is going to be produced at room temperature, the number density of the plasma can be found by the ideal gas law:

$$n = \frac{P}{kT} \tag{2.1}$$

where n is the number density, N is the number of gas molecules, V is the volume of the gas, P is the pressure of the gas, k is the Boltzmann's constant and T is the temperature of the gas. For $p = 10^{-3}$ atm, the number density is $n = 2.5 \times 10^{16} \text{ cm}^{-3}$. For $p = 1$ atm, the number density is $n = 2.5 \times 10^{19} \text{ cm}^{-3}$. There are several types of ionization that can be used to create plasma. The most common techniques used in the lab include thermal ionization, photoelectric effect, and tunnel ionization.

Thermal Ionization: This phenomenon occurs when the temperature of the gas is increased, and therefore the energy involved in collisions increases. The kinetic energy of particles involved in collisions must exceed the ionization energy of the atoms to knock out electrons and ionize them. Sufficiently energetic free electrons can then further ionize other atoms through collisions.

Photoelectric Effect: The photoelectric effect is when electrons are emitted from atoms after absorption of photons of specific energy. During the process, energy is transferred from the photon to the electron. For the process to occur, the energy of the photon has to be greater than or equal to the work function of the atom, i.e. the binding energy of the electron. In the case where there is excess energy, it gets converted to kinetic energy of the electron.

Tunnel Ionization: Using the classical theory of ionization, electrons would have to overcome their potential barriers in order to escape an atom, which is the case in the photoelectric effect. However, according to quantum mechanics, as long as the potential barrier is not infinite, the probability of finding an electron in the region of high potential barrier is small but not zero! This means if the potential barrier can be reduced, the probability of an electron tunneling through the barrier and escaping the atom increases. This can be done by introducing an intense electric field, which is usually an intense laser source.

When the laser field is very intense it can distort the potential of an atom in such a way that the potential barrier binding an electron is completely suppressed. This phenomenon is called barrier suppression ionization (BSI). This happens when the laser's electric field equals the Coulomb electric field experienced by the electron in a simple Bohr model of the atom. In PWFA experiments, we use tunnel ionization and not BSI. This is because tunnel ionization requires less laser energy and still works well to ionize the gas target. Tunneling ionization is overall easier and more efficient than BSI.

In past PWFA experiments, Lithium gas was used as the plasma source, and in that case it was difficult to control the longitudinal density profile of the plasma, since the Lithium gas was ionized by the electron drive bunch itself. This is possible because the ionization energy of Lithium is only 5.4 eV [4], which is quite low. Helium, by comparison, has a high ionization energy of 24.6 eV [5]. Hence, we decided to switch to using Helium gas to form our plasma source as it will not be ionized by the electron beam, allowing us to fully control the ionization profile through optical means by the appropriate focusing of an intense laser.

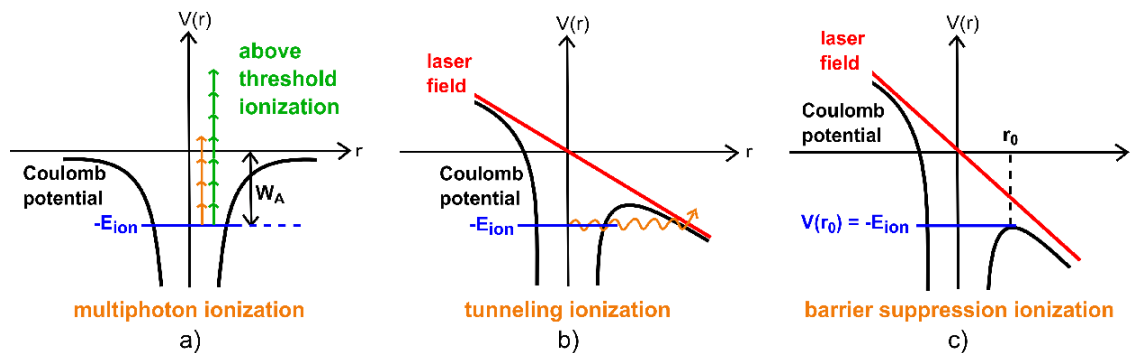


Figure 2.1: Different types of ionization [6]. Left: photo-ionization. Middle: tunnel ionization. Right: barrier suppression ionization.

2.2 Laser Ionization

Thermal ionization is not ideal for PWFA because it is difficult to control the plasma density profile, so instead we turn to ionization via laser pulse. We can precisely tailor the intensity profile of the laser pulse that is going to be used to create the plasma by using the appropriate optics. This, in turn, allows us to accurately control the density profile and the width of the ionized gas plasma source. This is a big advantage since this will enable us to maintain the electron bunch quality.

In order to create the plasma profile we are aiming for, we shoot a high intensity laser pulse into a cloud of gas. This causes the atoms of the gas to undergo ionization. There are two kinds of ionization that can take place in such conditions: photoelectric effect and tunnel ionization. To ionize the volume of plasma that is required, a high intensity laser pulse is required, which generally restricts us to the infrared wavelength regime. In this regime, tunnel ionization strongly dominates over photo-ionization. To

photo-ionize a Helium atom, we will need N photons such that

$$E_{He} \leq \frac{Nhc}{\lambda} \quad (2.2)$$

where E_{He} is the first ionization energy of Helium, h is the Plank's constant and λ is the wavelength of the photons emitted by the laser. Our IR laser has a wavelength of 800nm, so about 16 photons would be needed to ionize the Helium atoms, and thus the probability of all these photons hitting the atoms at the same time and causing photo-ionization is less than the probability of electrons escaping the atoms through tunnel ionization in this regime.

It is important to take into account the reflective properties of the plasma to ensure that our laser will be able to propagate as intended through the high intensity focal region where the gas is to be ionized. Using equation 1.1, we find that $w_p = 2.8 \times 10^{13}$ and $w = 2.4 \times 10^{15}$. Hence, we are in the $w_p < w$ regime and the laser pulse will be able to propagate through the plasma without being reflected away.

Chapter 3

Motivation

3.1 FACET II

One of the main goals for the Facility for Advanced Accelerator Experimental Tests (FACET) at Stanford Linear Accelerator Center (SLAC) was to conduct PWFA research. FACET was operated as a Department of Energy (DOE) user facility from April 2012 to April 2016. Now, FACET-II, the follow-on facility to FACET, has been commissioned in 2022. FACET-II has gone through major updates to allow us to achieve new goals such as preservation of beam quality and emittance [7]. Figure 3.1 shows an overhead view of the facility. (Note: the image was generated in 2019, at which time the facility had not yet begun operation.) Figure 3.2 shows the setup inside the accelerator tunnel. A beam of electrons will be sent from the electron source (bottom left) to the experimental area (bottom right), where it will arrive with an energy of 10 GeV per particle. The design allows for adding the capability to produce and accelerate

positrons (bottom, red line) at a later date.



Figure 3.1: Overhead photo of the FACET-II facility at SLAC National Accelerator Laboratory. Image taken from <https://facet-ii.slac.stanford.edu/>

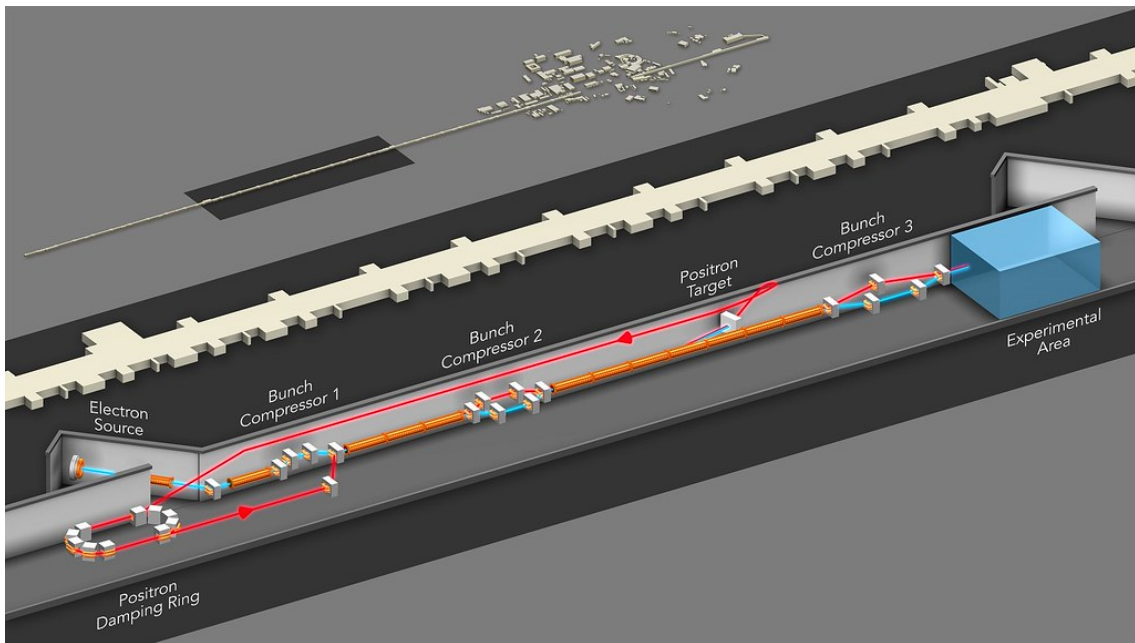


Figure 3.2: CAD drawing of the FACET-II accelerator tunnel. Image taken from <https://facet-ii.slac.stanford.edu/>

In FACET, the plasma source was created using a Lithium oven. Heat was applied to solid Lithium to vaporize it. Using Lithium for the plasma source was very convenient since it is very easy to ionize. All of the Lithium gas was ionized by the electron bunch alone without the need to use a laser, which implies the density profile was controlled

by the vapor profile of the Lithium, i.e. by thermodynamics only. As a result, it was difficult to control the plasma density profile, which is important for beam emittance preservation.

Therefore, in FACET-II, the plasma source is created by laser-ionizing low pressure Helium gas at room temperature in a vacuum chamber. Because Helium is much harder to ionize, ionization by the electron beam can be avoided and the plasma density profile will be determined entirely by the laser intensity pattern. The laser focusing can then be manipulated to the right intensity profile that will produce the plasma density profile needed to preserve the witness electron beam emittance [8, 9, 10].

3.2 Tandem Lens Scheme

Our goal is to produce a plasma filament with a target density on the order of 10^{16} – 10^{17} cm⁻³, a width of $> 200\mu\text{m}$, and a length of about 1m by laser ionization of Helium gas [11]. Former University of Colorado Boulder PhD student Dr. Robert Ariniello designed a sophisticated optical scheme to produce just the right focus to ionize such a filament of He with a 10 TW Ti:sapphire laser pulse. It uses a pair of custom diffractive lenses that he designed and tested. Each lens is 50 mm x 50 mm x 1 mm and costs \$6,000 to fabricate. They are now installed at FACET-II and are waiting to be used when the electron beam is ready for PWFA experiments.

Figure 3.3 shows the schematic of the tandem lens focusing technique. The first lens shapes the intensity of the laser before it reaches the second lens. The second lens removes the residual phase from the first lens and adds the required phase to produce a non-diffracting Bessel beam [11].

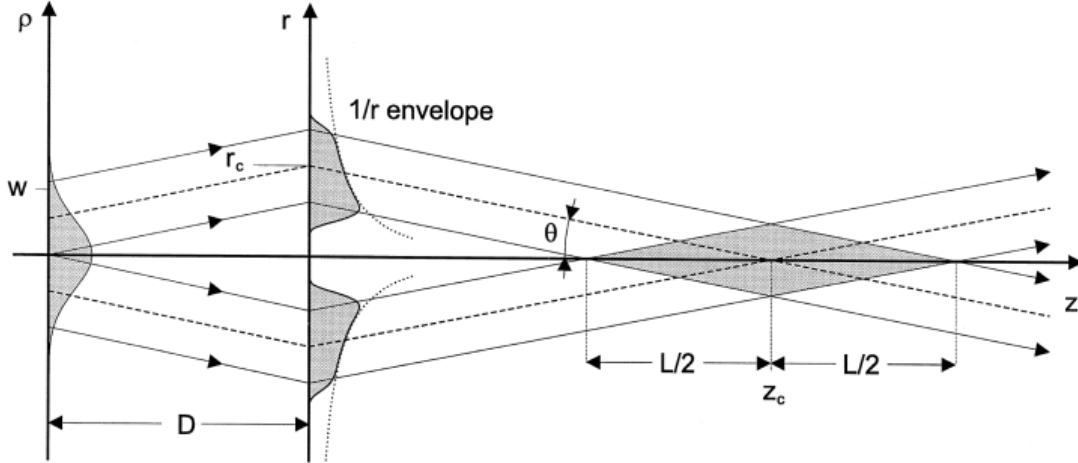


Figure 3.3: Schematic of the tandem lens focusing technique. The first lens (ρ) shapes the transverse donut intensity profile and the second lens (r) removes the residual phase from the first lens. The plasma forms at the shaded grey region downstream of the second lens where the Bessel beam is formed [11].

3.3 Axicons Lens Scheme

In this project, we explore the use of axicon lenses in place of the much more expensive and fragile diffractive lenses created by Dr. Ariniello. The tandem lenses create a Bessel beam focus that starts about 1.75m downstream from the second lens and extends for about 80cm, which is the full length needed for the PWFA experiments. My work explores the possibility of using axicon lenses to achieve a similar laser intensity

profile to that produced by the diffractive tandem lenses. The advantage of using axicons is that they are readily available (i.e. no need for custom fabrication) and are significantly cheaper (\$700 to \$1000 total cost).

Using one axicon would be sufficient if we only cared about achieving the Bessel beam intensity profile. However, we would like the Bessel beam to start 1.75m downstream from the axicon. This is important to prevent the axicon from damage by direct contact with very hot plasma.

One way to attain our preferred beam profile is to replace the incoming circular “flat-top” laser beam with a donut-shaped one. This would ensure that the Bessel beam is created some distance downstream from the axicon. As it happens, a pair of axicons can be used to create a donut intensity profile from a flat-top intensity profile. Thus, a set of three axicons is used in this project: a two-axicon telescope to create a collimated donut beam and a third axicon to create the long Bessel beam starting 1.75m downstream.

Chapter 4

Optics Of Axicons

4.1 Axicon Focusing

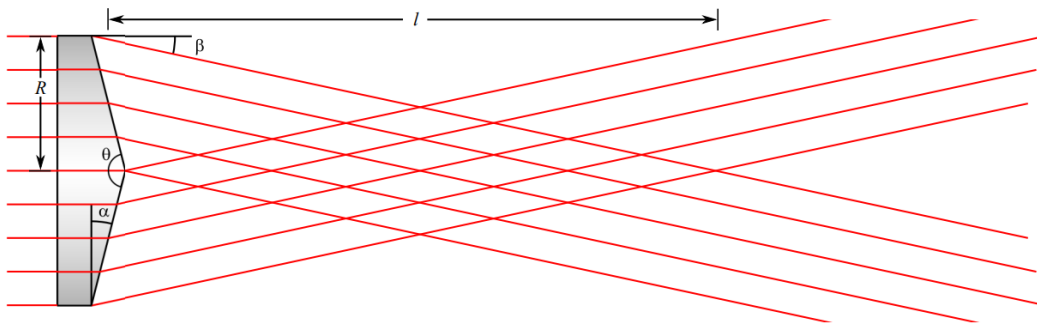


Figure 4.1: Ray tracing schematic of the focusing pattern of an axicon lens.

Axicons are conical-shaped optics that are characterized by the angle of the prism α and the outer radius R . However, for practical purposes, we let R be the outer radius of the incoming beam instead, since it is being used more frequently in calculations. All incoming parallel rays are focused by the axicon toward the central axis at the same angle.

Axicons are special optics that allow an incoming beam of light to be focused along length l instead of a single focal point as in the case of a more conventional spherical lens. The deflection angle of the rays β is determined from α and the index of refraction of the axicon. Using Snell's Law:

$$\beta = \arcsin\left(\frac{n_a}{n} \sin \alpha\right) \quad (4.1)$$

where n is the index of refraction of the medium surrounding the axicon and n_a is the index of refraction of the axicon. Since we did our experiments in air and the axicon is made of glass, we can plug in $n = 1$ and $n_a = 1.5$. By rearranging the equation and applying the small angle approximations (since we will be working with $\alpha = 0.5^\circ$ and $\alpha = 1^\circ$) we get:

$$\beta \approx \frac{\alpha}{2} \quad (4.2)$$

The end of the focal length is given by:

$$z_{end} = \frac{R}{\tan \beta} \approx \frac{2R}{\alpha} \quad (4.3)$$

For a donut-beam, the start of the focal length is given by:

$$z_{start} \approx \frac{2r_{inner}}{\alpha} \quad (4.4)$$

where r_{inner} is the inner radius of the donut-beam. Hence, the full length of the Bessel beam generated by donut-beam is:

$$l = z_{end} - z_{start} \approx \frac{2}{\alpha}(R - r_{inner}) \quad (4.5)$$

The intensity along the focal length of the axicon is not uniform. The longitudinal intensity profile created by a flat-top beam grows linearly along the z -axis until the full focal length of the Bessel beam is reached:

$$I(z) = I_{peak}z/l \quad (4.6)$$

where I_{peak} is the peak intensity at the end of the focus. Because each annulus at initial radius r is focused to a successive value in $z(r) = 2r/\alpha$, and the energy in each annulus is given by:

$$dE(r) = I(r)\tau\pi r dr \quad (4.7)$$

where τ is the laser pulse duration in time. Figure 4.2 shows how the longitudinal intensity profile of a Bessel beam generated by a flat-top beam, where the intensity is constant across all radii, $I(r) = I_0$.

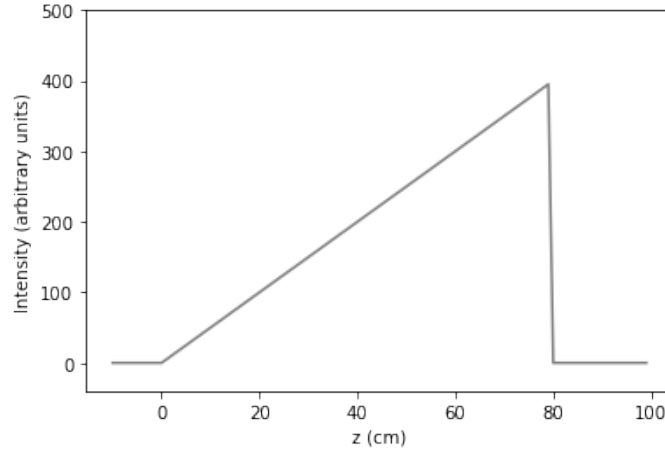


Figure 4.2: Axial intensity profile of a Bessel beam formed by a flat-top laser beam when focused by an axicon lens.

On the other hand, the longitudinal intensity profile formed by a more realistic super-Gaussian flat-top beam tends to drop down more gradually near the end of the focus. The transverse intensity of a super-Gaussian beam is:

$$I(r) = I_0 e^{-\left(\frac{r}{w}\right)^m} \quad (4.8)$$

where w is the beam width factor and m is the degree of the super-Gaussian. Hence, each annulus has energy:

$$dE(r) = I(r) \tau \pi r dr = I_0 e^{-\left(\frac{r}{w}\right)^m} \tau \pi r dr \quad (4.9)$$

Figure 4.3b shows a 4mm diameter super-Gaussian laser beam propagating from left to right through an axicon of angle $\alpha = 0.7^\circ$. Figure 4.3a represents the longitudinal intensity profile of the propagating laser beam in the figure below it. Figure 4.3c shows the transverse intensity profile of the Bessel beam generated at the position of the peak longitudinal intensity which is at about $z = 250\text{mm}$. The transverse intensity profile is given by:

$$I(r, z) = I_{peak}(z) \left[J_0 \left((n_a - 1) \alpha \frac{2\pi}{\lambda} r \right) \right]^2 \quad (4.10)$$

where $I_{peak}(z)$ is the longitudinally varying peak intensity of the laser, n_a is the refractive index of the axicon, λ is the central wavelength of the laser beam and r is the radial distance from the center of the beam at the z location where the Bessel beam is being measured.

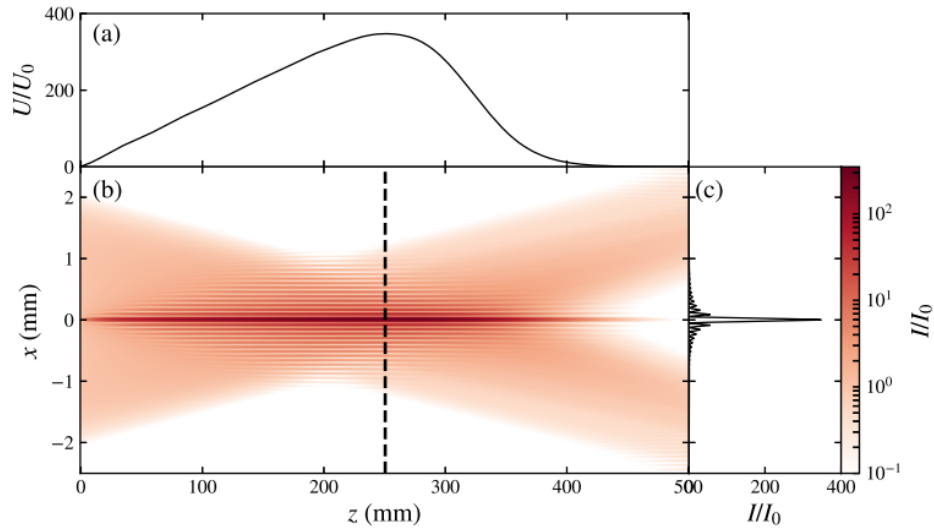


Figure 4.3: Axial intensity profile (a), transverse intensity profile (b), and transverse intensity lineout (c) produced by a super-Gaussian laser beam focused by an axicon lens.

4.2 Optical Kerr Effect

The Kerr effect is a nonlinear optical effect that causes a change in the refractive index of a material in response to an applied electric field. The optical Kerr effect is the case when the electric field is due to the light itself. This causes a variation in index of refraction which is proportional to the local intensity of the light. The total index of refraction of a material is given by:

$$n = n_0 + n_2 I \quad (4.11)$$

where n_0 is the refractive index with the absence of intense light or laser beam, n_2 is the second-order non-linear refractive index, and I is the local intensity of the beam. This refractive index variation is responsible for the nonlinear optical effects of self-focusing

and self-phase modulation [12].

Self-focusing is a phenomenon that occurs when a medium whose index of refraction increases when an intense beam of light passes through it acts like a focusing lens. In this scenario, the peak intensity of the light continues increasing in a feedback loop. The process stops when the beam finally starts to defocus or the medium is damaged. This effect is detrimental because it can alter the intensity profile of our laser beam which will in turn affect the density profile of the PWFA plasma source. Further, self-focusing can damage the optics used in the experiment [13].

Self-phase modulation occurs when varying refractive index induced in a medium causes a phase shift in the beam, thus leading to a wider pulse frequency spectrum. This effect can cause a reduction in intensity and may lead to the plasma being insufficiently ionized, i.e. the plasma density or width may be lower than the targeted density and width [14].

In order to quantify the nonlinear phase-shift of light, we use the B-integral which is defined by:

$$B = \frac{2\pi}{\lambda} \int_0^L n_2 I(z) dz \quad (4.12)$$

where L is the thickness of the lens and $I(z)$ is the optical intensity along the beam axis [15]. When the B-integral is low, n_2 and $I(z)$ can be approximated as constant in the medium of the lens, and the integral can be simplified into:

$$B = \frac{2\pi}{\lambda} n_2 I \Delta z \quad (4.13)$$

Chapter 5

Experimental Setup and Methods

5.1 Triple Axicon Design

In order to achieve the desired plasma profile according to what has been discussed in the previous chapters, we came up with the triple axicon design that is shown in Figure 5.1.

The design consists of two axicons which act like a telescope to create a laser pulse that has a donut-shaped transverse profile. As the incoming laser pulse passes through the first axicon, it produces a Bessel beam just after the optic. The light rays then diverge to form a ring or donut-shaped pulse. In this process, the wavefront of the pulse becomes tilted. The second axicon removes the wavefront tilt created by the first axicon returning it to flat again and the beam is collimated. For this reason, the second axicon has to have exactly the same angle as the first axicon, otherwise it wouldn't

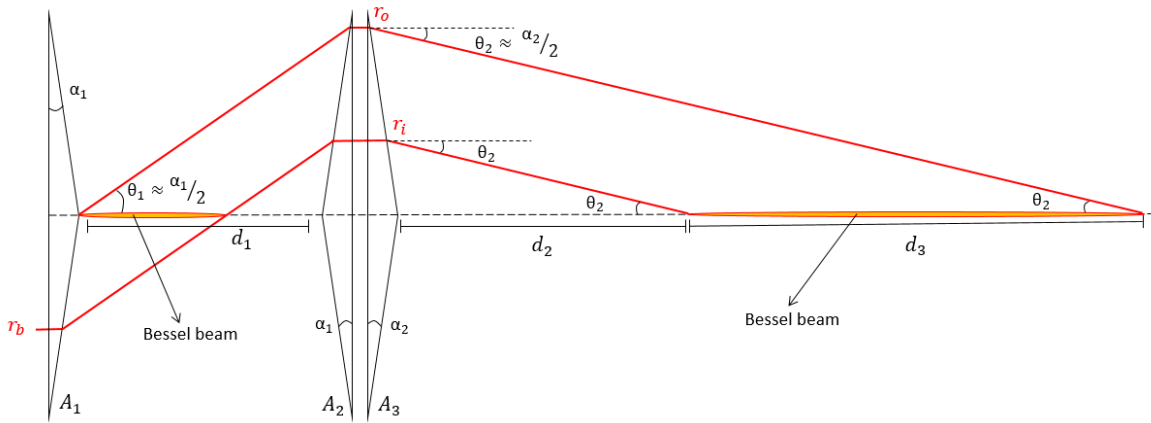


Figure 5.1: Schematic of the triple axicon design. The first two axicons form a telescope that creates a donut-shaped beam which is focused a distance d_2 downstream from the third axicon. The telescope axicons are characterized by the same angle α_1 and the third axicon is characterized by angle α_2 .

exactly cancel the initial tilt. The donut beam then goes into the third axicon with an initially flat wavefront, making the behavior of the third axicon very easy to predict and calculate.

The modular aspect of this design (i.e. the telescope and the focusing axicon) allows for flexibility in implementing the setup. For instance, we can choose distances d_1 , d_2 and d_3 according to what fits in our work station best and find the respective angles that can generate a Bessel beam at the chosen location. Ease of execution also comes in handy when the design needs to be set up at a different laboratory.

Setup Calculations

Before I lay down the calculations for figuring out the magnitudes of all the parameters in our design, I would like to discuss the restrictions that we imposed on the design. First, we would like our incoming beam to have a radius $r_b = 20\text{mm}$ just like the laser beam at FACET-II. However, our calculations have shown that the total longitudinal length of the setup will exceed 4m and we only have a distance of 3m to work with at the lab ($d_1 + d_2 + d_3 \leq 3\text{m}$), therefore, we decided to reduce the size of the incoming beam that we will be testing to $r_b = 15\text{mm}$. Second, the targeted length of the plasma is about 80cm, hence $d_3 = 800\text{mm}$. Third, the axicons available in the lab have a diameter of 50mm, which suggests that the outer radius of the donut-beam r_o should be less than 25mm. We chose to work with $r_o = 20\text{mm}$. Axicons $A1$ and $A2$ have $\alpha = 0.5^\circ$ and axicon $A3$ has $\alpha = 1^\circ$.

Now, we need to find d_1 and d_2 , the distance between $A1$ and $A2$ and the distance between $A3$ and the start of the Bessel beam, respectively. By using equations 4.3 and 4.4 and applying our constraints we get that $d_1 = 230\text{cm}$ and $d_2 = 35\text{cm}$. Note that R is r_b and $r_b = r_o - r_i$ where r_i is the inner radius of the donut-beam. A summary of all the parameters and their magnitudes is given in the table below:

Table 5.1: Triple axicon setup parameters.

Parameter	Parameter Value
r_b	15mm
r_o	20mm
d_1	230cm
d_2	35cm
d_3	80cm
α_1	0.5°
α_2	1°

5.2 Experimental Setup

Figure 5.2 shows a schematic of the experimental setup. For this project, a low power HeNe laser ($\sim 2\text{mW}$) was used to test the triple axicon optical scheme. This is especially useful because it provides us with the opportunity to study all aspects of the design with a safe, visible laser before implementing the setup with a high power Ti:Sapphire laser. We wanted to work with a laser beam that had a radius of 20mm to imitate the beam radius that is going to be used in FACET II Experiments. The HeNe outputs a laser beam of about 1mm radius, so we attached a beam expander onto it, but we ended up with a beam size that is a bit bigger than we wanted. Therefore, we used a convex lens telescope to rectify the beam size.

Since we don't have enough table space to setup the experiment in a straight line, we used two mirrors to enable us to bend the pathway of the laser so that we can have a total of 3m of longitudinal distance to work with. The first axicon is placed around

30cm downstream from the second convex lens. The total longitudinal distance between the first two axicons is about 2.3m. As Figure 5.2 shows, two mirrors were used between the axicons to fold the laser path back to conserve table space. The second axicon is immediately followed by the third axicon which in turn focuses the donut-beam along the axis of the rail camera. The distance between the third axicon and the start of the rail is 15cm and the rail length is 120cm. We took snapshots of the Bessel beam from 15cm to 115 cm downstream of the third axicon ($15\text{cm} < z < 115\text{cm}$). The first two axicons are characterized by $\alpha = 0.5^\circ$ and the third axicon is characterized by $\alpha = 1^\circ$

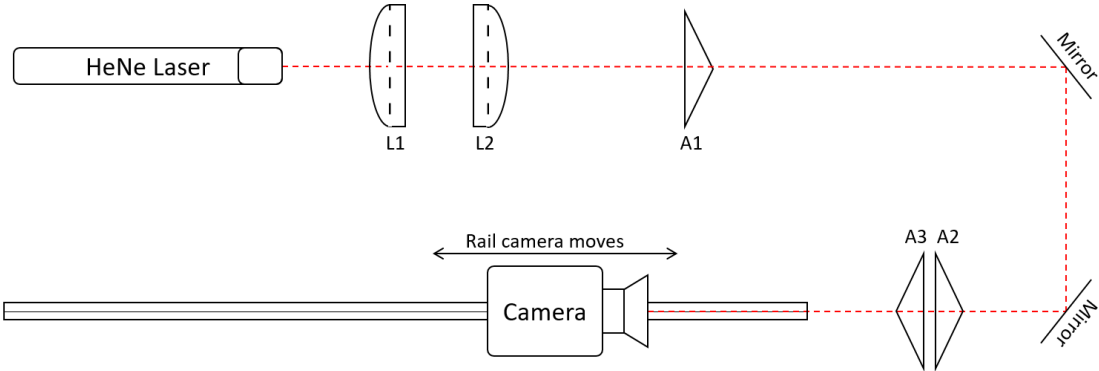


Figure 5.2: Experimental setup schematic. The HeNe laser has the expander attached to it (small square from which the laser beam is emitted). L_1 and L_2 are convex lenses. A_1 , A_2 and A_3 are axicons. The camera sits atop a rail on which it can move along the laser propagation axis.

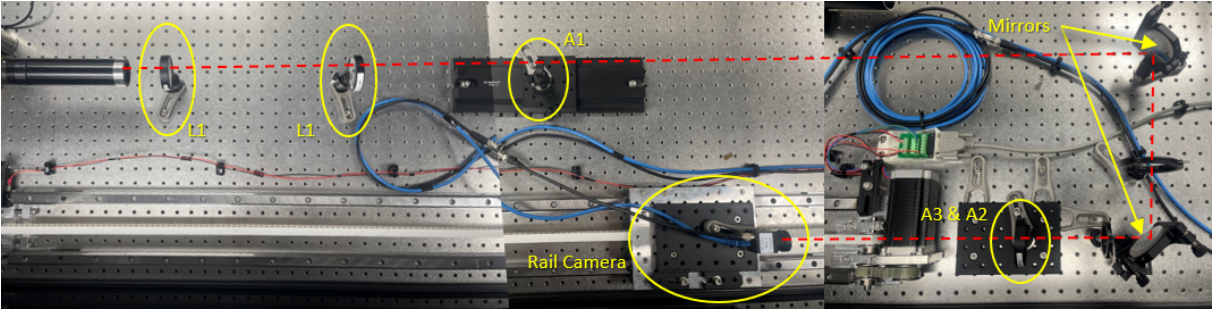


Figure 5.3: Photograph of the experimental setup in the CU Boulder laser lab.

Our primary diagnostic was a moveable CMOS gigabit ethernet camera that sits on a rail and can be controlled by the data acquisition system (DAQ). We referred to this as the “rail camera”. After setting up the experiment, we gathered data about the quality of our Bessel beam by sliding the camera along the rail from $z = 15\text{cm}$ to $z = 115\text{cm}$ in 5cm intervals, taking three snapshots of the beam at each position.

5.3 Method of Studying Alignment Tolerance

There are two types of tolerance studies that were performed on the triple axicon setup. The first measured how well the setup can withstand inaccuracies in the transverse (vertical) displacement of the optics as shown in Figure 5.4 and the second measured sensitivity to inaccuracies in the angular displacement of the optics as shown in Figure 5.5.

The way we performed this study is by taking snapshots of the Bessel beam when the axicon is misaligned. We used the optimal alignment that we could achieve as the reference. Vertical misalignment was measured by a ruler and angular misalignment

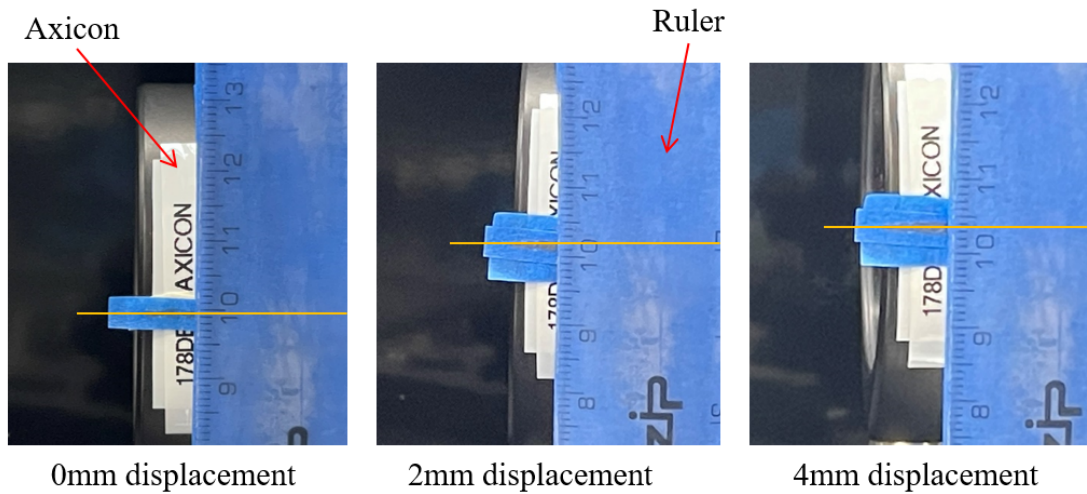


Figure 5.4: Testing for vertical displacement of the optics. The orange line in each image represents the height measurement of the optic. The first image shows that the original height of the axicon is ~ 10 cm. The second image shows the height of the axicon to be ~ 10.2 cm (2mm displacement). The third image shows the height of the axicon to be ~ 10.4 cm (4mm displacement).

was measured by a protractor. The qualifying features for what was considered in tolerance were the presence of a single-peaked Bessel beam and the correct length of the focal region.

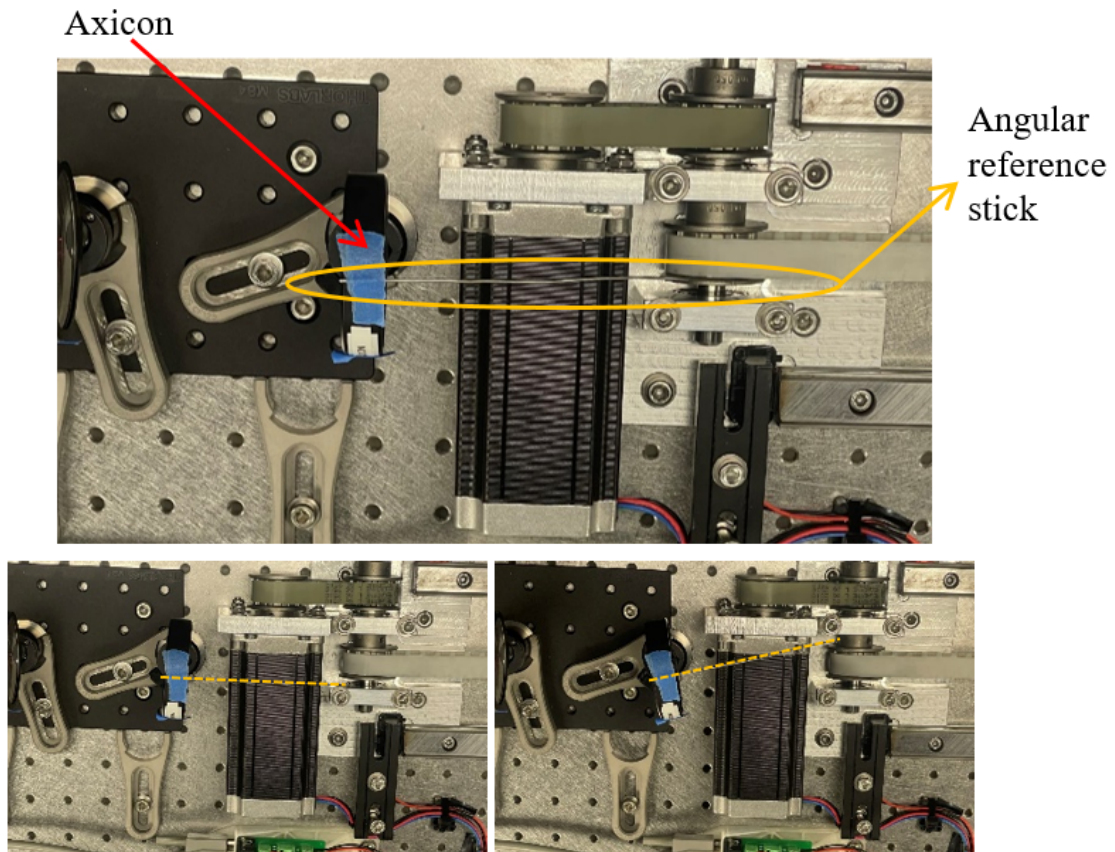


Figure 5.5: Testing for angular displacement of the optics. A stick was taped to the axicon to tell which direction it faced in optimal alignment. Protractor software was used to measure the angle in the images. The directions of the two axicons are highlighted with dashed orange lines.

Chapter 6

Data and Results

6.1 Best Alignment Laser Profile

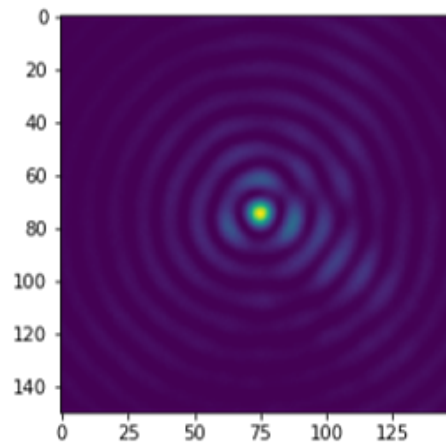


Figure 6.1: Transverse intensity profile for the Bessel beam under optimal alignment conditions measured at $z=35\text{cm}$ (35cm downstream from the third axicon). This corresponds to the position of the peak intensity.

Figure 6.1 shows the Bessel beam intensity profile after optimizing the alignment of the optics. The first part of the analysis considers how well the Bessel beam intensity

profile matches our prediction. To do this, we take a lineout across the image at the location of the peak intensity, since the Bessel beam is at its best form here (Figure 6.2). According to our data, the position of the peak intensity is at $z = 35\text{cm}$. As we can see from Figure 6.3, the observed transverse intensity profile matches our theoretical prediction. Fits to the Bessel profiles using Equation 4.10 yield $\alpha = 1.3^\circ$, which agrees well with our expectations based on the experimental setup.

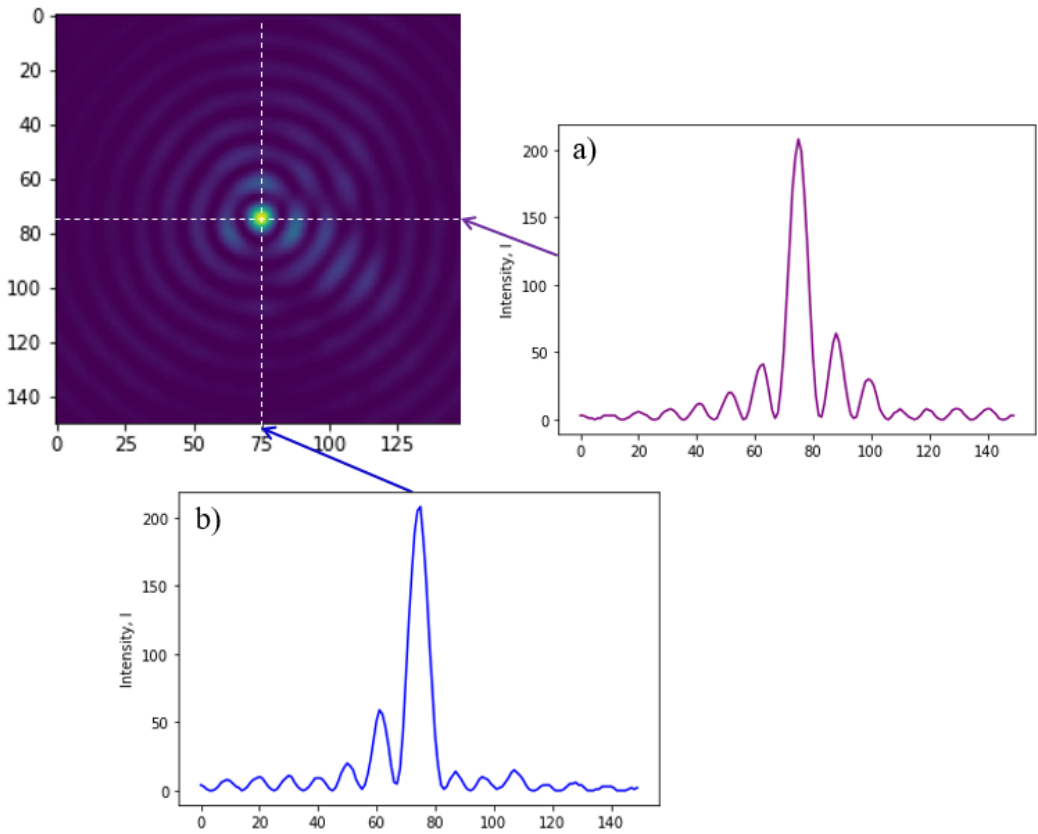


Figure 6.2: Transverse intensity profile for the Bessel beam (top left). Plots generated by taking the lineout across the (a) row and (b) column that have the highest intensity (pixel count).

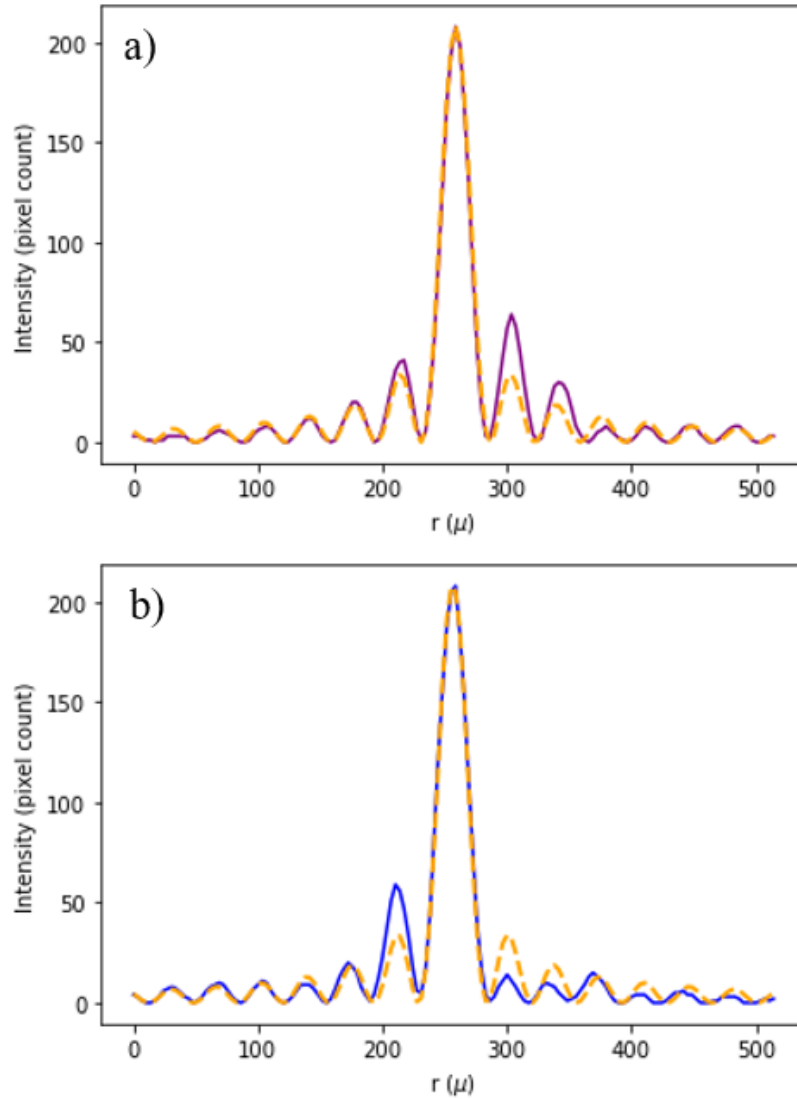


Figure 6.3: Horizontal (a) and vertical(b) intensity lineouts (solid lines) of the optimized Bessel beam profile taken from 6.1. A fit to the Bessel profile is shown (orange dashed lines) in each, with a result of $\alpha = 1.3^\circ$ in both plots.

In addition, we measured the peak intensity as a function of distance from the third axicon. The results of this measurement are shown in Figure 6.4. We expected the region of the axial intensity to ramp up, then maintain a somewhat flat region of high intensity and then ramp back down. The aspect of the intensity growing and dying slowly is important for generating the plasma density ramps that are critical for preserving the electron beam emittance in the PWFA.

According to Figure 6.4, we achieved our goal of producing a high intensity region that tends to increase and decrease slowly at the ends. However, the steepness of the ramps was not quite ideal—the upstream ramp was a bit too steep while the downstream ramp was a bit too shallow. This is not unexpected, however, because the HeNe laser we used for our experiment emits a Gaussian beam instead of a flat-top beam. Our design assumed that a flat-top beam will be used, because that is a better description of the the high-intensity Ti:sapphire laser that will be used both in our lab and in the FACET-II experiments to form the PWFA plasma source.

We expected the Bessel beam region to start 35cm downstream from the third axicon ($z = 350\text{mm}$) and ended at $z = 1150\text{mm}$, as seen in Figure 6.4a by the orange vertical lines. Our results show that our Bessel beam started at $z = 150\text{mm}$ and ended at about $z = 950\text{mm}$, as seen in Figure 6.4b by the green vertical lines. We achieved the goal of producing an 80cm-long Bessel beam, though it was shifted about 20cm upstream of where we expected it. Again, this is primarily a result of our calculations being done based on the assumption of a flat-top beam instead of a Gaussian beam.

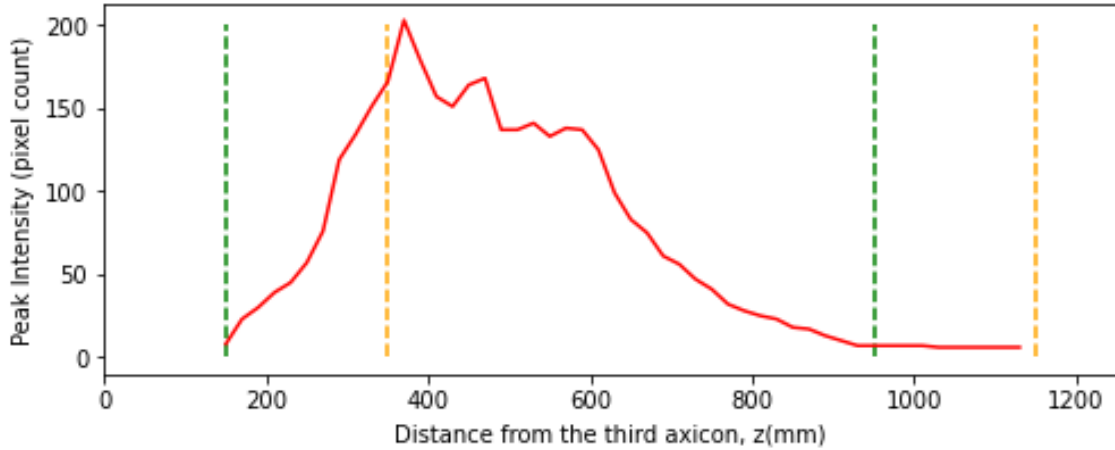


Figure 6.4: Measured longitudinal intensity profile of the Bessel as measured along the length of the camera rail. The vertical dashed lines indicate the start and end of the expected Bessel beam (orange vertical lines) and the actual resultant Bessel beam (green vertical lines).

We also measured the FWHM (full width at half-maximum) of the central intensity peak as a function of distance along the z -axis. The z -axis is along the rail, where $z = 0$ at the final axicon A3 lens and positive values of z indicate a distance downstream of the lens. Figure 6.5 shows the FWHM of the central beam using both horizontal and vertical lineouts. The FWHM remains relatively constant over the region of interest, where the peak intensity is high, which is located between $z = 300\text{mm}$ and $z = 700\text{mm}$. Both plots agree that the FWHM in the high intensity region are about $25 - 28 \mu\text{m}$. We conclude from the data that the laser is well collimated entering the final axicon, indicating that the axicon telescope lenses have well-matched angles α and are well aligned.

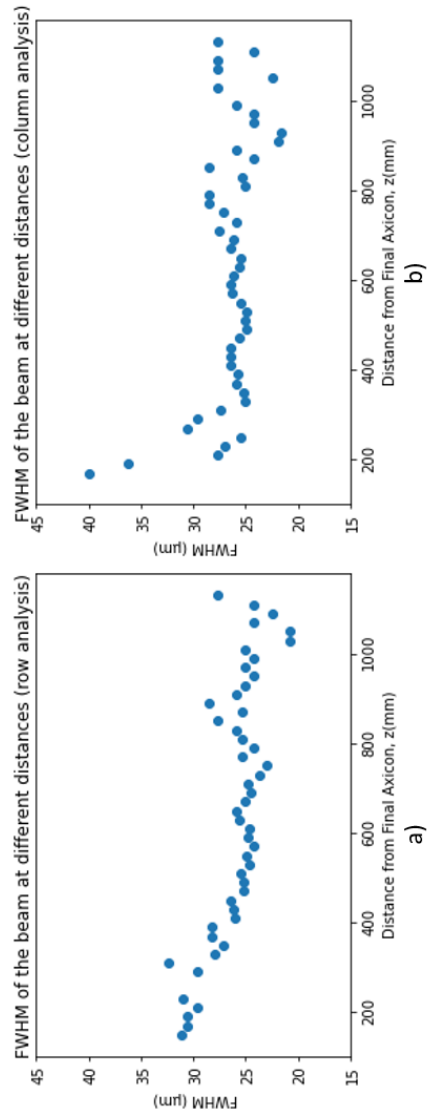


Figure 6.5: FWHM of the central Bessel lobe as measured along the z-axis using horizontal (a) and vertical (b) lineouts.

6.2 Tolerance Studies Results

The tolerance studies have shown that we can maintain a Bessel beam intensity profile when the optics are vertically and angularly displaced from the optimal alignment height and angle by $\pm 3\text{mm}$ and 10° respectively. An example of the aberration caused by vertical displacement of the third axicon is shown in Figure 6.6.

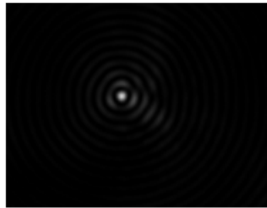

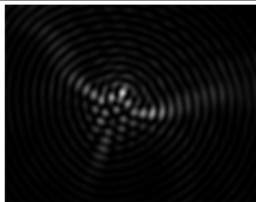
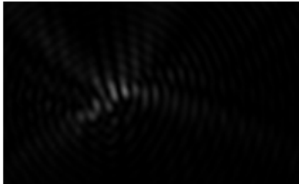
Displacement from the center (mm)	Beam image
0	
+3	
+5	
-5	

Figure 6.6: Laser intensity profile measurements for various vertical displacements of the third axicon.

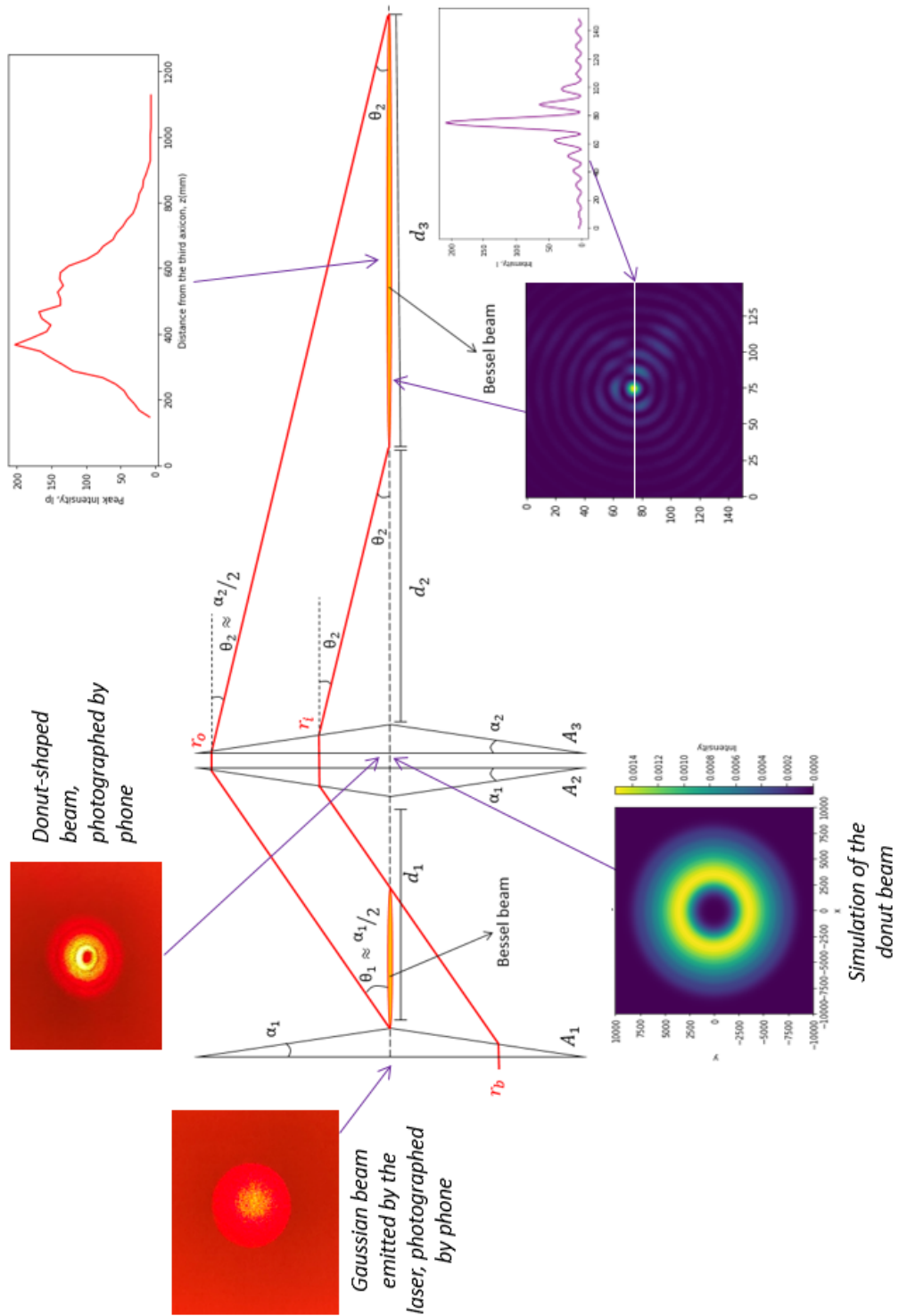


Figure 6.7: Summary of the major findings of the experiment.

Chapter 7

Conclusions and Future Work

7.1 Conclusions

Our results imply that the triple axicon setup can provide the focusing features required to produce an optimal plasma source for use in PWFA experiments at FACET-II. Further, our work demonstrates the effectiveness of using first-order optics in the triple axicon design process in order to achieve our targeted intensity profile. Finally, our measurements show that the setup has forgiving tolerance to small deviations from the optimal alignment which means that it can handle minor misalignment errors.

7.2 Potential Issues

The laser pulse in the triple axicon setup may have to pass through a substantial amount of glass, which indicates that the Kerr effect may take place and hence may

lead to intensity loss through self-phase modulation.

To avoid this, the value B-integral should be kept low, i.e. it should not exceed 3-5. After performing the B-integral calculations on the setup used in our experiment, we found that the B-integral for the high-intensity Ti:sapphire laser pulse would be approximately 14, which is far too large. Therefore, a new configuration with fewer (and thinner) axicons that will reduce the B-integral must be found.

One way we can use fewer axicons is to use two axicons instead of three. The second and third axicons will be replaced with single axicon that performs the same function as the original two combined. The scaled up setup of our original design would have had axicons $A1$ and $A2$ with $\alpha = 8^\circ$ and axicon $A3$ with $\alpha = 4^\circ$. The new version, with axicons $A2$ and $A3$ replaced with a single axicon would have $\alpha = 12^\circ$. Note, that the replacement axicon is characterized by $\alpha = 8^\circ + 4^\circ$, which is the combined angles of $A2$ and $A3$. This makes sense, since we want to have the same amount of refraction and we are working in the small angle limit.

Another potential challenge is the ability of the laser to form a plasma filament when it goes through a focus between the first two axicons. This plasma could affect the propagation of the laser in an unpredictable way before it reaches the final focusing optic. To avoid this, the first axicon can be replaced with a defocusing axicon. This will prevent the formation of plasma between the first two axicons by directly creating a donut intensity profile without needing to first send the laser through a focus.

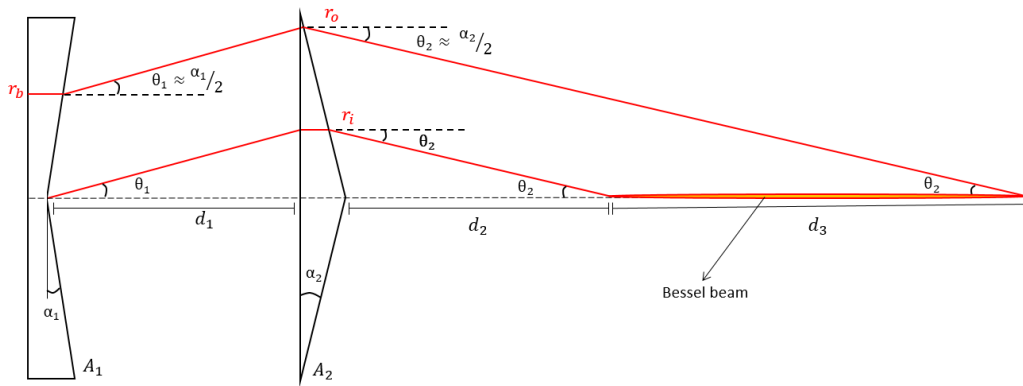


Figure 7.1: Schematic of the new double axicon design. The first axicon defocuses the light into a donut-shaped beam which is then focused a distance d_2 downstream from the second axicon. Axicon A_1 is characterized by angle α_1 and axicon A_2 is characterized by angle α_2 .

7.3 Future Work

The next step is to test the new axicon design using the HeNe laser. In case the investigation of the new setup proved that it is potentially viable, we can move on to testing the scaled up version of the design on the IR laser that we have at the CU laser lab at CU Boulder before applying and testing the setup at FACET-II. Otherwise, we will need to come up with a new novel design that could help us achieve our goal at costs much lower than the tandem lens scheme.

Bibliography

- [1] Joshi, C. (2006). Plasma accelerators. *Scientific American*, 294(2), 40-47.

- [2] Gschwendtner, E., & Muggli, P. (2019). Plasma wakefield accelerators. *Nature Reviews Physics*, 1(4), 246-248.

- [3] Gibbon, P. (2020). Introduction to plasma physics. arXiv preprint arXiv:2007.04783.

- [4] Connor, N. (2020). Lithium - Ionization Energy. Periodic Table. <https://www.periodic-table.org/Lithium-ionization-energy/>

- [5] Connor, N. (2020). Helium - Ionization Energy. Periodic Table. <https://www.periodic-table.org/helium-ionization-energy>

- [6] Krainov, V. P. (1995). Theory of barrier-suppression ionization of atoms. *Journal of Nonlinear Optical Physics & Materials*, 4(04), 775-798.

- [7] Yakimenko, V., Alsberg, L., Bong, E., Bouchard, G., Clarke, C., Emma, C., ... & Yocky, G. (2019). FACET-II facility for advanced accelerator experimental tests. *Physical Review Accelerators and Beams*, 22(10), 101301.
- [8] Litos, M. D., Ariniello, R., Doss, C. E., Hunt-Stone, K., & Cary, J. R. (2019). Beam emittance preservation using Gaussian density ramps in a beam-driven plasma wakefield accelerator. *Philosophical Transactions of the Royal Society A*, 377(2151), 20180181.
- [9] Ariniello, R., Doss, C. E., Lee, V., Hansel, C., Cary, J. R., & Litos, M. D. (2022). Chromatic transverse dynamics in a nonlinear plasma accelerator. *Physical Review Research*, 4(4), 043120.
- [10] Ariniello, R., Doss, C. E., Hunt-Stone, K., Cary, J. R., & Litos, M. D. (2019). Transverse beam dynamics in a plasma density ramp. *Physical Review Accelerators and Beams*, 22(4), 041304.
- [11] R. Ariniello (2022). Emittance Preservation in a Plasma Wakefield Accelerator, 160-168.
- [12] Paschotta, R. Kerr Effect. *RP Photonics-Encyclopedia of Laser Physics and Technology*.
- [13] Vaziri, M. R. (2015). Comment on “Nonlinear refraction measurements of materials using the moiré deflectometry”. *Optics Communications*, 357, 200-201.

[14] Paschotta, R. (2007). Self-phase Modulation. RP Photonics-Encyclopedia of Laser Physics and Technology.

[15] Paschotta, R. B integral. RP Photonics-Encyclopedia of Laser Physics and Technology.